

METAL DUSTING IN A LABORATORY ENVIRONMENT – ALLOYING ADDITION EFFECTS

B. A. BAKER, Special Metals Corporation, Huntington, West Virginia
G. D. SMITH, Special Metals Corporation, Huntington, West Virginia

ABSTRACT

Long-term testing of a wide variety of nickel-base and iron-base alloys has been conducted in an environment generated by an inlet gas composition of CO-20% H₂ at 621°C. Some degree of metal dusting attack has been observed for all alloys tested. Multivariate analysis has been performed, in order to determine the effects of various alloying additions upon the mass loss rate and the pitting progression rate. The results indicate the beneficial effects of a nickel-base alloy matrix, scale-forming element additions, and the presence of certain carbide-forming elements upon alloy performance.

INTRODUCTION

Metal dusting has been responsible for considerable losses in equipment and production time across numerous industries including petrochemical processing, direct iron-ore reduction and heat treating. The phenomenon termed “metal dusting” can be described as a catastrophic form of carburization which occurs under conditions where the carbon activity of the gaseous atmosphere is greater than one and can result in rapid metal wastage, producing pits and grooves as the affected metal disintegrates into a mixture of powdery carbon and metal particles.

CAUSES AND THERMODYNAMIC CONSIDERATIONS

Consider stream reforming as an example of a process in which metal dusting can occur. The combination of natural gas, or methane, with steam at high temperature produces a mixture of gases commonly referred to as ‘syngas’ which contains mostly H₂, CO, CO₂, H₂O and some CH₄. When such gas mixtures are present in the process stream in the critical temperature range of about 450° to 800°C, metal dusting can be a severe corrosion problem (Jones and Baumert, 2001). Figure 1 shows equilibrium constants versus temperature for a few reactions which are capable of producing carbon in such a gas mixture. The reaction for cracking of butane, while not predicted to have significance in the typical syngas environment, has been included in Figure 1 for the purpose of illustrating the likelihood for the occurrence of metal dusting within a solely hydrocarbon-based environment. Within the syngas environment, the two reactions contributing most to carbon deposition are: 1.) the reduction of CO by hydrogen and 2.) The decomposition of CO₂ (the Boudouard reaction). The fact that the equilibrium constant for each of these reactions dips below one at about 750°C helps to explain why metal dusting activity within syngas environments is typically observed in the temperature range of about 450°C to about 800°C (the lower temperature boundary being determined by reaction kinetics).

The need for greater efficiency has reduced the quantity of steam used for the reforming process, resulting in lower steam-to-hydrogen ratios. Higher front-end pressures have also

increased the CO content of the syngas. Lower H_2O/H_2 ratios in combination with higher CO/CO_2 ratios result in lower oxygen partial pressures and higher carbon activities, respectively, and serve to increase the severity of metal dusting attack. In addition, the use of advanced catalysts which are not tolerant to sulfur in the process stream, has necessitated the use of alloys which are more resistant to metal dusting, as sulfur-containing species can be added to the process stream in order to mitigate the problem. Avoidance of metal dusting is often accomplished in industry by designing around the critical temperature range. Syngas is produced at temperatures above the critical range ($>800^\circ C$) and transferred to a boiler via a short transfer line where it is rapidly quenched to temperatures below the critical metal dusting range ($<450^\circ C$). Alloy ferrules that are used in the transfer line do often experience metal dusting and are periodically replaced. The need to maximize the efficiency of steam reforming technology has led to the development of equipment which must be capable of operating within the range of temperature and carbon activity which can promote metal dusting. This necessitates the use of materials which exhibit excellent resistance to metal dusting attack.

An adherent, protective, healable oxide surface layer is required for protection of an alloy against metal dusting attack. Although oxide formation may be stable, the oxide layer may still be susceptible to disruption. Higher levels of the scale forming element will then make the scale healing process more rapid and complete. Figure 2 illustrates the pO_2 required to form various metal oxides at $627^\circ C$. Additions of particular interest obviously include silicon, aluminum and chromium. Ultimate resistance to metal dusting may involve complex interactions of scale characteristics, diffusivity of scale-forming elements and carbon through the alloy matrix and carbon saturation limits.

EXPERIMENTAL

Table 1 shows the chemical composition for each alloy tested. Test specimens were prepared from commercially available material; sample dimensions were approximately 2.5cm X 2.5cm X thickness. Samples were ground to a 120-grit finish for standardization purposes.

Samples were exposed at $621^\circ C$ in a horizontal electrically-heated furnace having a mullite tube, in an atmosphere generated from an inlet gas mixture of CO-20% H_2 . Samples were cycled, lightly brushed, ultrasonically cleaned in methanol and weighed at two-week intervals. In addition to mass change, pitting depth was also determined for each sample using an optical microscope having a calibrated fine focus knob.

RESULTS

Figure 3 illustrates the mass loss rate as a function of time. The maximum pit depth as a function of time is plotted in Figure 4. Table 2 shows the pit progression rate for each alloy tested. Figure 5 shows the result of multiple regression analysis of the log of the pit progression rate, calculated by averaging the pit depth over the total testing duration, versus a summation of the weight percentage of various alloying additions. The summation coefficients were based upon the regression results. Only the austenitic nickel-base alloys and Fe-Ni-Cr alloys were included in this calculation; the ferritic alloy, MA956, and also alloy 400 were excluded. The best fit was produced using the following summation (multiples of weight percentage):

$$(\text{Ni} + \text{Co}) + 2\text{Cr} + 5\text{Mo} + 9\text{Ti} + 11\text{Si} + 23\text{Al} - 1\text{Fe}.$$

This same regression technique was used to characterize the variation in the log of the mass loss rate with the percentage of certain alloying additions (Figure 6). Again, only the austenitic nickel-base and Fe-Ni-Cr alloys were included in the calculation. The best fit was obtained using the following summation:

$$(\text{Ni} + \text{Co}) + 5\text{Mo} + 11\text{Cr} + 15\text{W} + 52\text{Ti} + 54\text{Al} + 83\text{Si} - 1.5\text{Fe}.$$

As a general trend, nickel-base alloys exhibited lower mass loss rates and pitting progression rates than iron-base alloys. Alloys 600 and MA754, which contain only 15% and 20% chromium, respectively, were exceptions and had a fairly high mass loss rate resulting from numerous, albeit fairly shallow, pits. Neither of these alloys other significant additions of scale-forming or carbide-forming elements. Alloy 690 (Ni-29Cr-9Fe), commonly used as heat-exchanger tubing in the nuclear industry, exhibits much lower mass loss and pit progression rates than alloy 601, which is increasingly used as an upgrade from iron-base materials such as Cr-Mo steels, austenitic stainless steels and Fe-Ni-Cr heat-resistant alloys such alloy 800. Figure 7 shows photomicrographs of a pit in the alloy 690 sample in cross section after 14160 hours of testing. Etching the sample electrolytically in methanol-5% HNO₃ revealed the characteristic 'white layer' near the pit surface, presumed to be saturated with carbide, in addition to the intergranular carbides extending beneath the white layer. The mechanically alloyed corollary to alloy 690, alloy MA758, also exhibits good performance. Alloy MA956, a ferritic alumina former, also exhibited good performance for a considerable incubation period of almost 12,000 hours after which pitting initiated and progressed quite rapidly. Figure 8 shows photomicrographs of a pit in the alloy MA956 after the total testing duration of 15,926 hours. Large carbides are evident after etching. The pitting progression also appears to be possible related to the orientation of the large grains. Alloy 263 performed well despite its modest chromium level of 20% and 39% iron content, and appears to possibly gain protection from its substantial titanium addition and possibly its molybdenum addition, which may promote early carbide formation and provide diffusional blocking of the carbon flux (Müller-Lorentz 1999). Figure 9 shows photomicrographs of the surface of the alloy 263 sample after 15, 936 hours of exposure. A thin layer of what is presumed to be carbide is evident at the surface, away from the pitted region. Alloy 617, having 22% chromium and 1.2% aluminum, may also gain the same benefit from its molybdenum addition. Figure 10 shows photomicrographs of the alloy 617 sample after 14,160 hours of exposure. As with the alloy 263, what is presumed to be a thin layer of carbide is present of the surface of the alloy 617 as well. Alloy 625LCF, a refined version of alloy 625, has performed reasonably well and contains 21.5% chromium, 9% molybdenum and 3.6% niobium and probably benefits from its fine grain structure. The high silicon content of alloy TD may have afforded some enhancement in performance, in addition to its 3% molybdenum content. Alloy 671, with its substantial chromium addition, is performing admirably, despite pitting activity initially to a depth of about 75 microns.

The best performer overall in the laboratory test was alloy 693, which possesses very high chromium and aluminum contents in combination with a high nickel alloy matrix. In-situ field

exposures under metal dusting conditions have confirmed this alloy's superior performance. Figure 11 shows a photomicrograph of a sample sectioned after 15,816 hours of testing.

CONCLUSIONS

Due to efforts to increase the efficiency of processes involving the production of syngas and development of advanced catalysts, metal dusting corrosion has become more prevalent. Failures of iron-base alloys as well as nickel-base alloys which contain insufficient levels of key alloying elements have prompted equipment designers to seek materials that are more resistant to metal dusting. Field and laboratory data confirm the desirability of addition of certain scale-forming and possibly carbide-forming elements in conjunction with a nickel-base alloy matrix to limit pit progression rates. Based upon the results of this study, the newly-developed alloy 693 offers the most promising potential for metal-dusting limited applications.

ACKNOWLEDGEMENTS

The authors would like to thank Chad Clary for testing and evaluation of the materials in this study.

INCONEL®, INCOLOY®, INCOTHERM™, MONEL®, NIMONIC®, and 625LCF® are trademarks of the Special Metals group of companies.

REFERENCES

- 1) Jones, R. T. and Baumert, K. L., Paper Number 1372, CORROSION/2001, Houston, Texas, 2001.
- 2) Müller-Lorentz, E. M., Proc. EUROCORR 1999, Aachen, Germany, September, 1999.

Table 1
Nominal Composition of Commercial Alloys (Weight Percent)

Alloy	Ni	Cr	Fe	Mn	Si	Al	Ti	C	Other
INCONEL® alloy MA754	78	20	-	-	-	0.3	0.5	0.05	0.5 Y ₂ O ₃
INCOTHERM™ alloy TD	73	22	-	-	1.4	-	-	0.01	3.0 Mo
INCONEL® alloy 600	72	15.5	8	0.3	0.3	0.3	0.3	0.08	-
INCONEL® alloy MA758	67	30	-	-	-	0.4	0.5	0.05	0.5 Y ₂ O ₃
MONEL® alloy 400	64	0.1	1.6	0.7	0.1	0.02	0.4	0.15	32.2 Cu
INCONEL® alloy 693	62	29	4	-	-	3.1	-	-	Nb, Zr
INCONEL® alloy 625LCF®	61	21.5	2.5	-	0.1	0.2	0.2	0.02	9 Mo, 3.6 Nb
INCONEL® alloy 601	60.5	23	13	0.2	0.2	1.4	0.4	0.05	-
INCONEL® alloy 690	59	29	9	0.2	0.1	0.3	0.3	0.02	-
INCONEL® alloy C-276	57	15.5	5.5	-	-	0.1	0.2	-	16 Mo, 3.8W
INCONEL® alloy 671	53	46	-	-	-	0.3	0.3	0.03	-
INCONEL® alloy 617	55	22	1	-	0.1	1.2	0.4	0.08	12.5 Co, 9 Mo
NIMONIC® alloy 263	51	20	39	0.3	0.1	0.5	2.2	0.06	20 Co, 5.9 Mo
INCOLOY® alloy 825	42	21.5	28	0.4	0.1	0.1	1	0.02	3 Mo, 2Cu
INCOLOY® alloy DS	37	16	41	1.0	2.3	-	-	0.08	-
INCOLOY® alloy 330	35	19	44	1.0	1.3	-	-	0.07	-
INCOLOY® alloy 803	34	27	36	1.0	0.8	0.4	0.4	0.08	-
INCOLOY® alloy 864	34	21	39	0.4	0.8	0.3	0.6	0.03	4.2 Mo
INCOLOY® alloy 800	32	21	45	0.9	0.1	0.4	0.4	0.07	-
INCOLOY® alloy MA956	-	20	75	-	-	4.5	0.5	0.05	0.5 Y ₂ O ₃

Table 2
Pitting Progression Rate after Exposure in CO-20% H₂ at 621°C

Alloy	Pit Depth		Exposure Time	Pit Progression Rate	Pit Progression Rate
	Mils	μm	Hours	Mils per Hour	μm/h
800	25.0	635	1056	2.37E-02	9.32E-04
330	17.0	432	1056	1.61E-02	6.34E-04
DS	24.0	610	2400	1.00E-02	3.94E-04
803	21.5	546	2400	8.96E-03	3.53E-04
825	7.0	178	1662	4.21E-03	1.66E-04
864	9.1	231	2184	4.17E-03	1.64E-04
601	19.8	503	6600	3.00E-03	1.18E-04
600	1.8	46	1392	1.29E-03	5.09E-05
MA956	18.6	472	15936	1.17E-03	4.60E-05
MA754	3.3	84	2936	1.12E-03	4.43E-05
TD	7.3	185	6728	1.09E-03	4.27E-05
263	17.0	432	15936	1.07E-03	4.20E-05
625LCF	6.3	160	6397	9.85E-04	3.88E-05
MA758	7.0	178	8023	8.72E-04	3.44E-05
690	12.1	307	14160	8.55E-04	3.36E-05
C-276	4.0	102	6397	6.25E-04	2.46E-05
671	3.6	91	8686	4.14E-04	1.63E-05
617	1.6	41	14160	1.13E-04	4.45E-06
693	1.7	43	15816	1.07E-04	4.23E-06

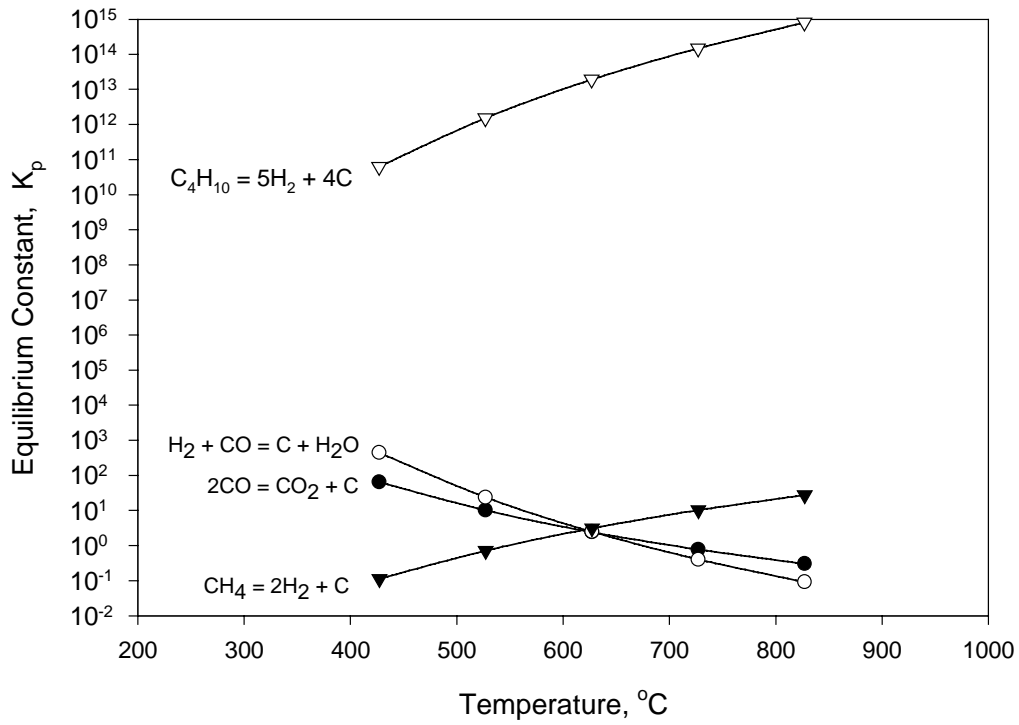


Figure 1. Equilibrium constants for reactions which may produce carbon in metal dusting environments.

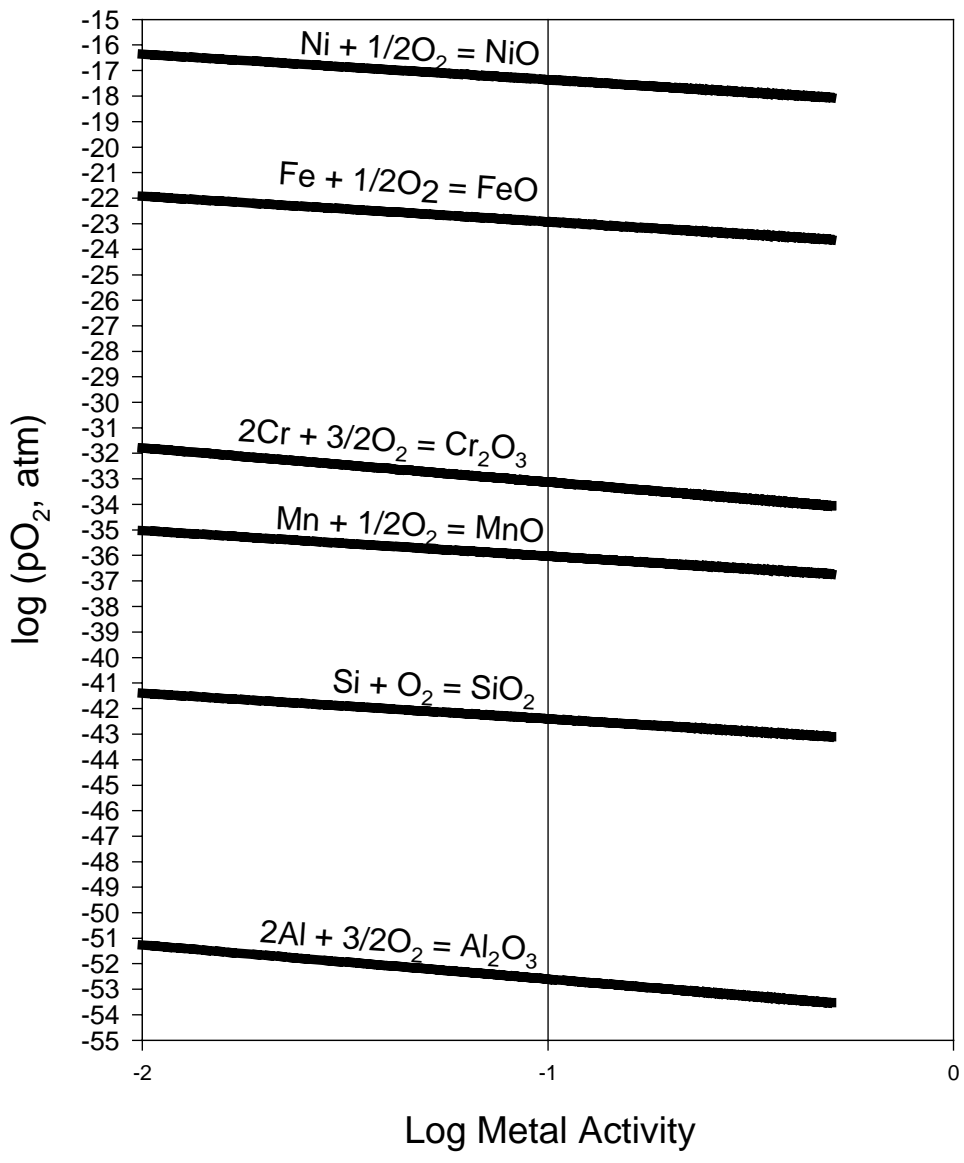


Figure 2. The log of oxygen partial pressure required for the formation of the most stable oxides of aluminum, chromium, nickel, manganese, and silicon as a function of metal activity at 627°C.

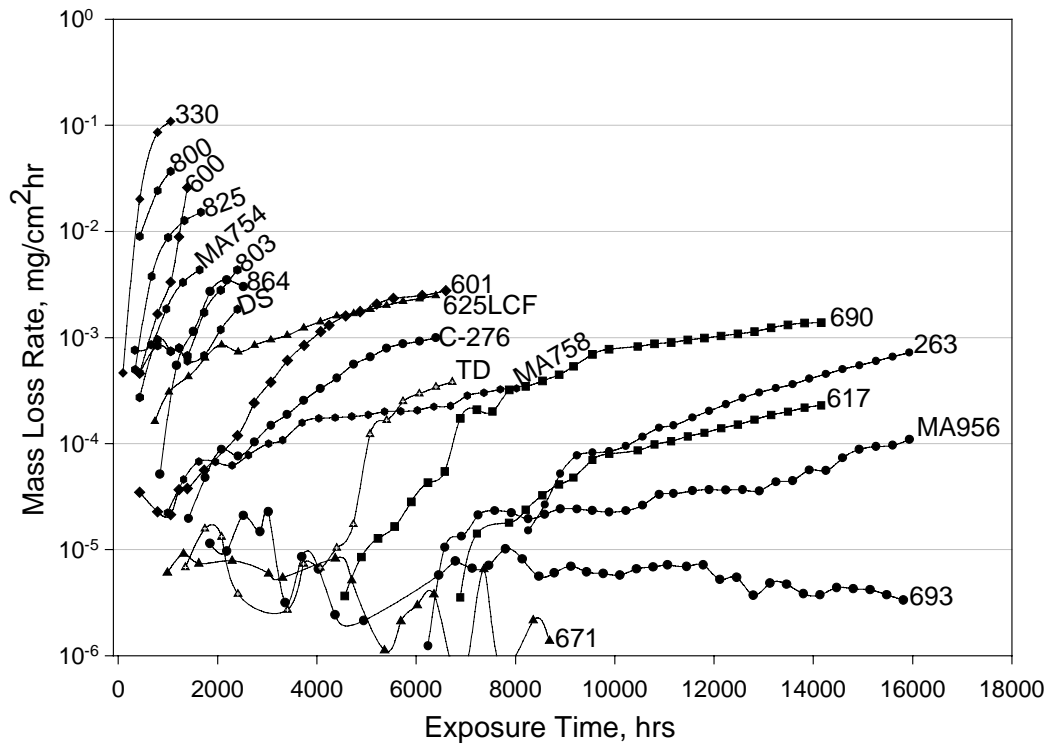


Figure 3. Mass loss rate versus exposure time for alloy samples exposed to CO-20% H₂ at 621°C.

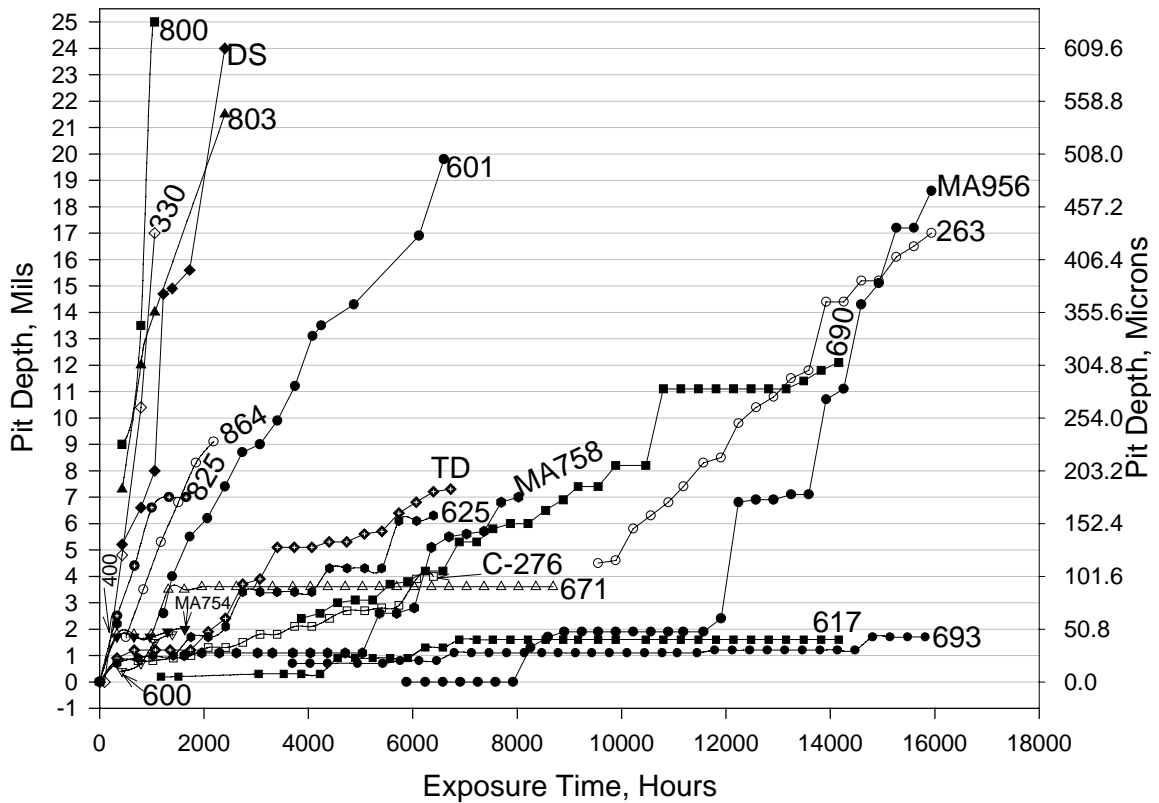


Figure 4. Maximum pit depth measurements for alloy samples exposed to CO-20% H₂ at 621°C.

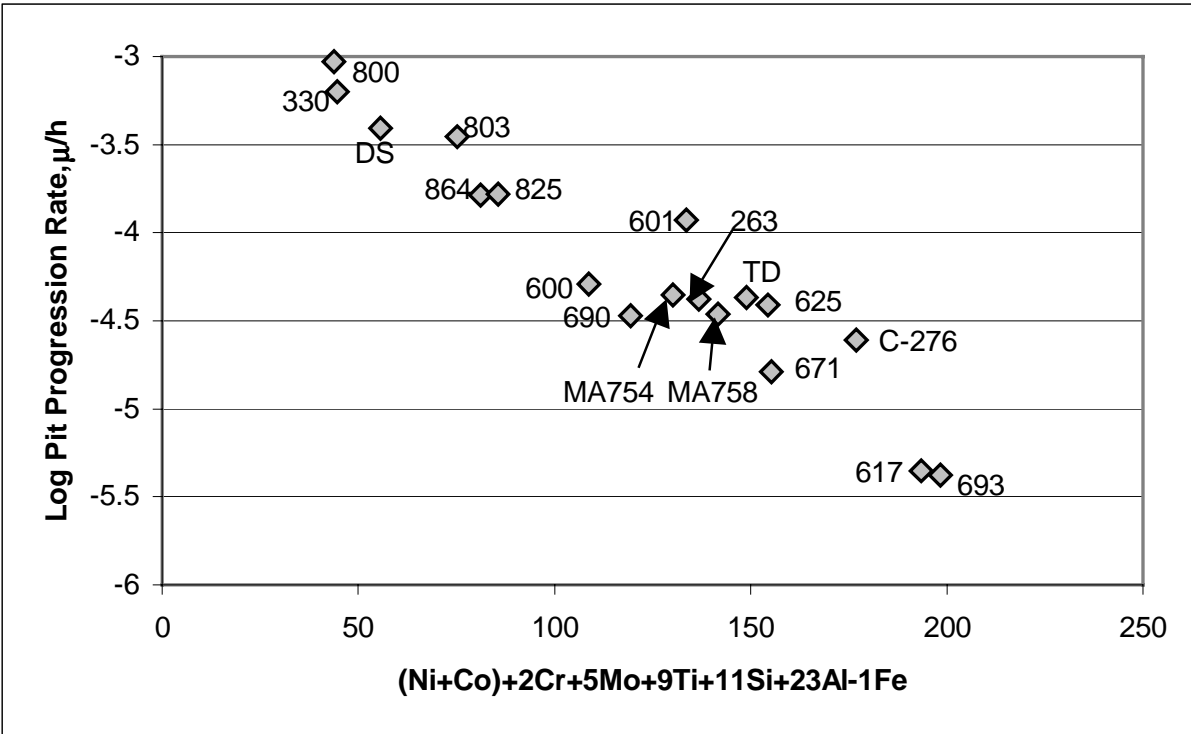


Figure 5. Results of multiple linear regression for pit progression rate versus composition.

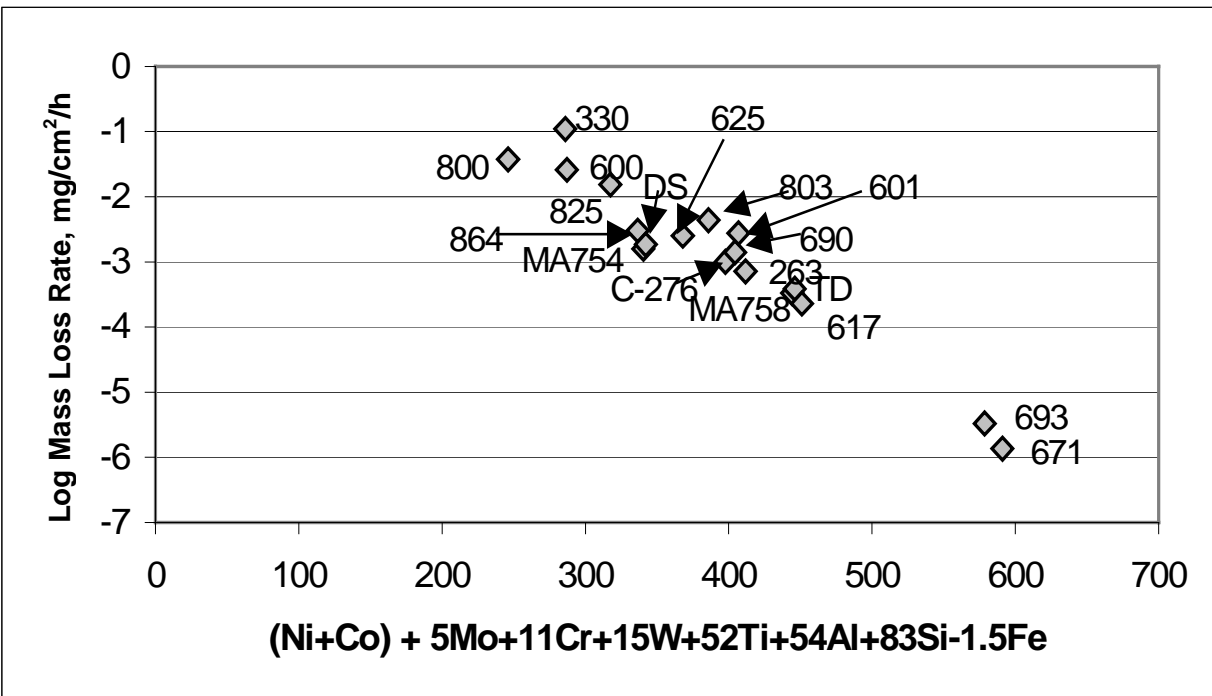


Figure 6. Results of multiple linear regression for log mass loss rate versus composition.

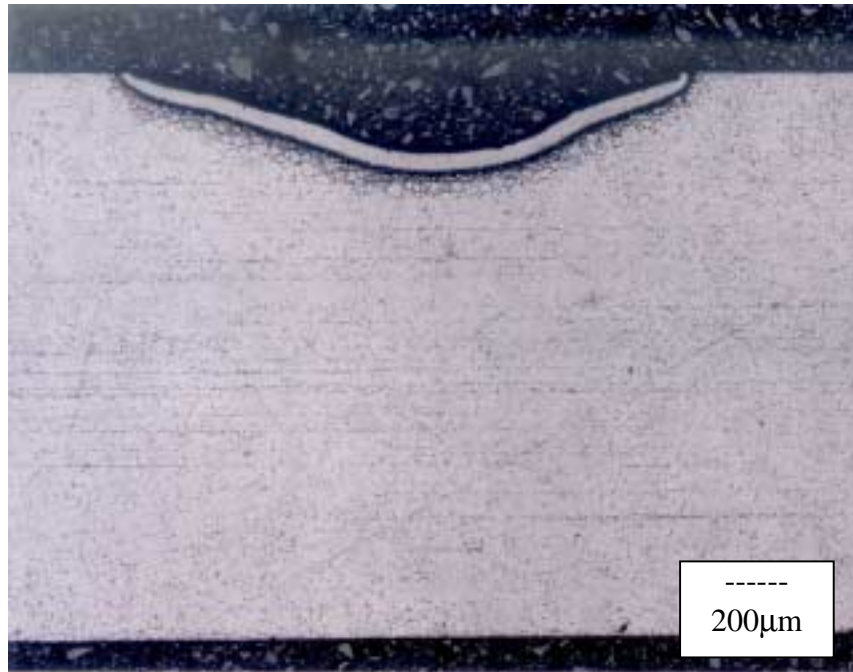
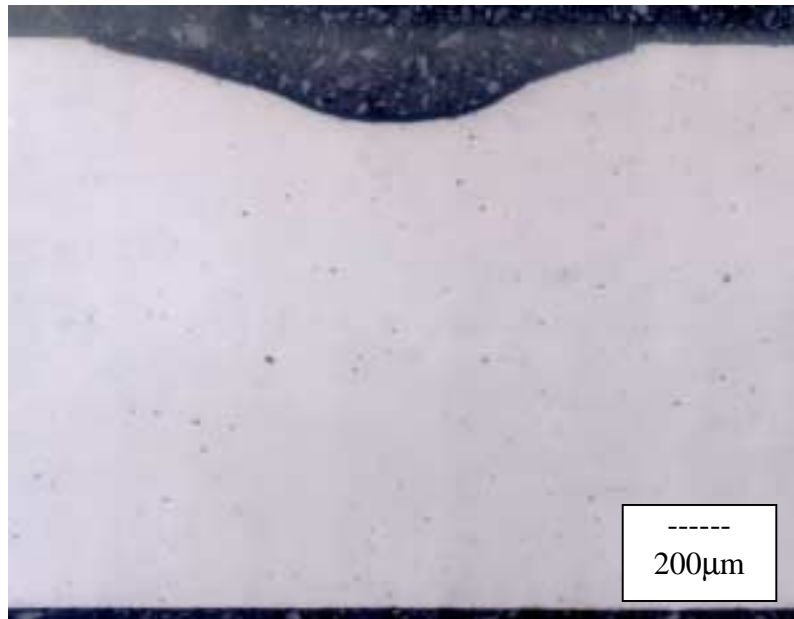


Figure 7. Photomicrographs showing a cross section of an alloy 690 sample exposed in CO-20% H₂ at 621°C for 14,160 hours. The top photo shows a pit in the unetched condition. The bottom photo shows the same are after electrolytically etching in methanol - 5% HNO₃.

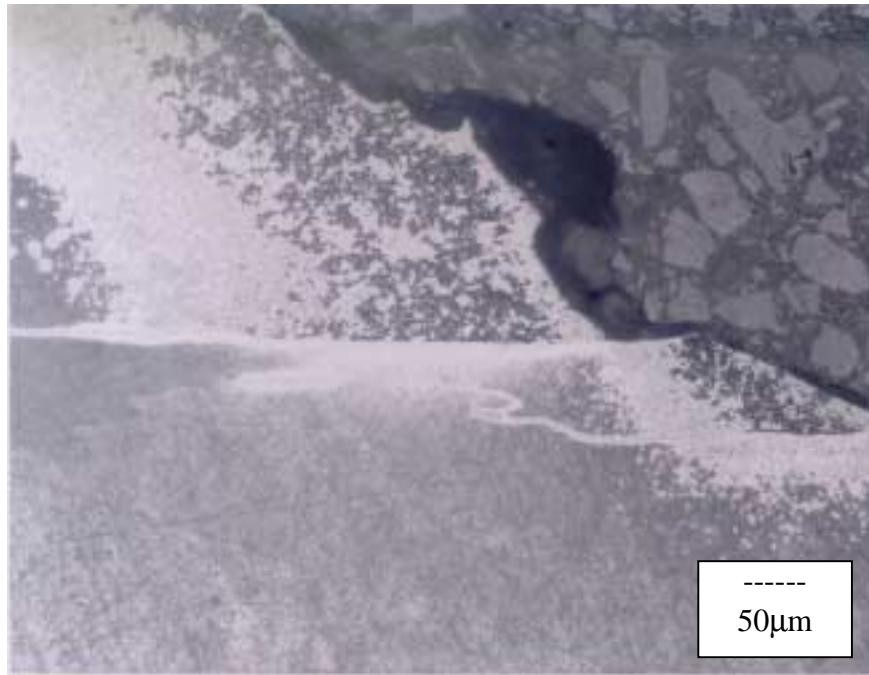
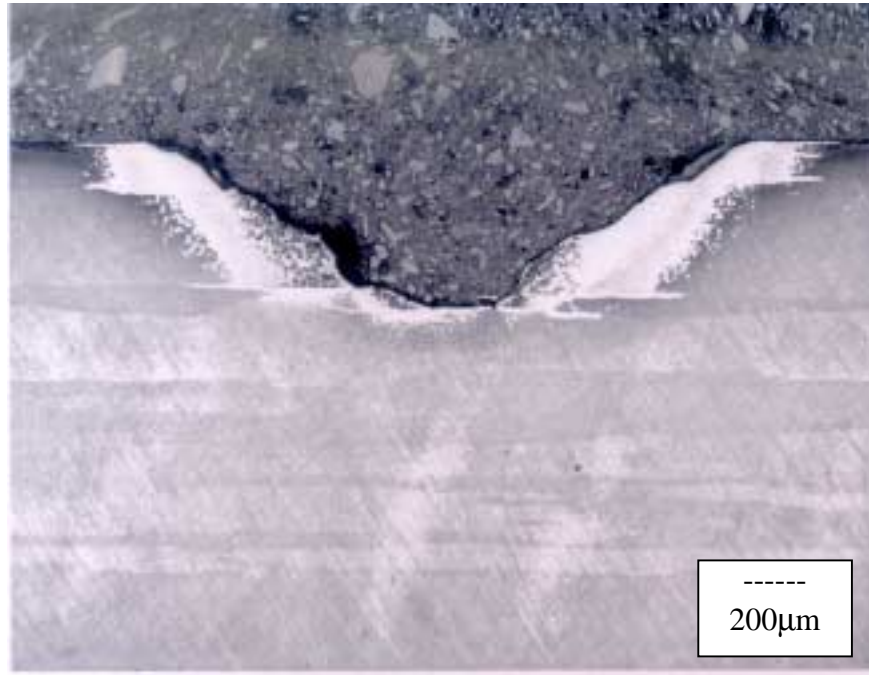


Figure 8. Photomicrographs showing alloy MA956 after 15, 936 hours of exposure in CO-20% H₂ at 621°C. The sample was electrolytically etched in methanol - 5% HNO₃.

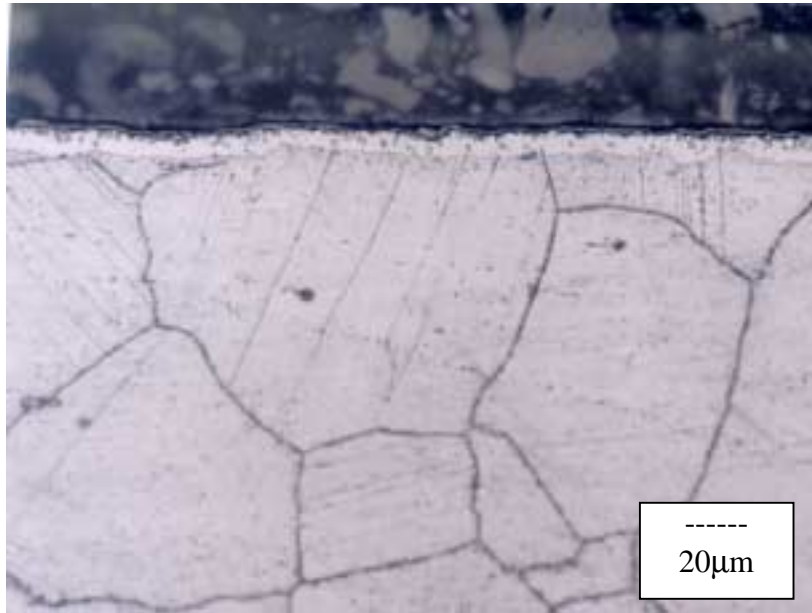
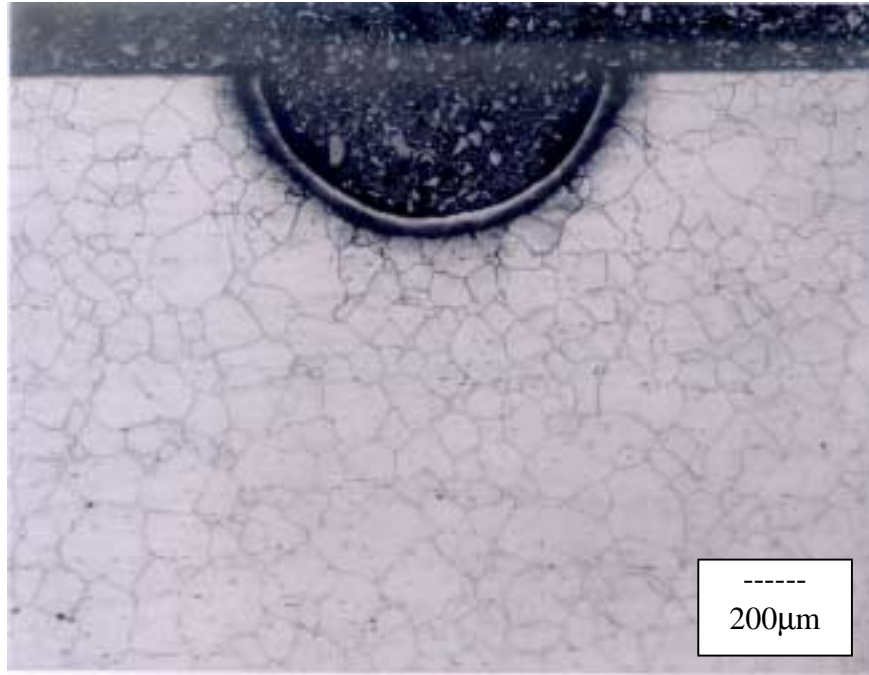


Figure 9. Photomicrographs showing alloy 263 after 15, 936 hours of exposure in CO-20% H₂ at 621°C. The sample was electrolytically etched in methanol - 5% HNO₃. The top photo shows the microstructure of a typical pit. In areas not affected by pitting, a distinct, thin surface layer is present.

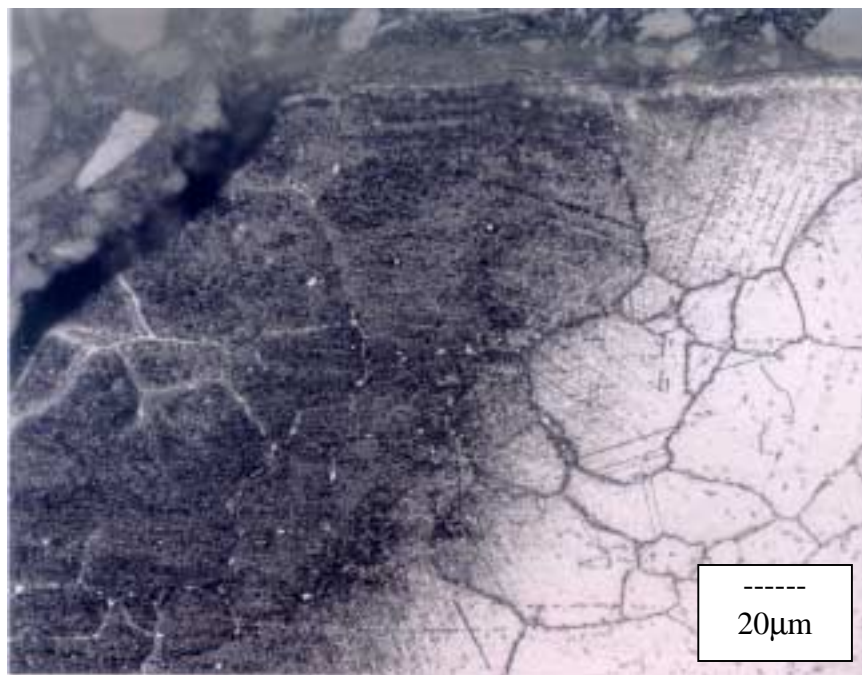
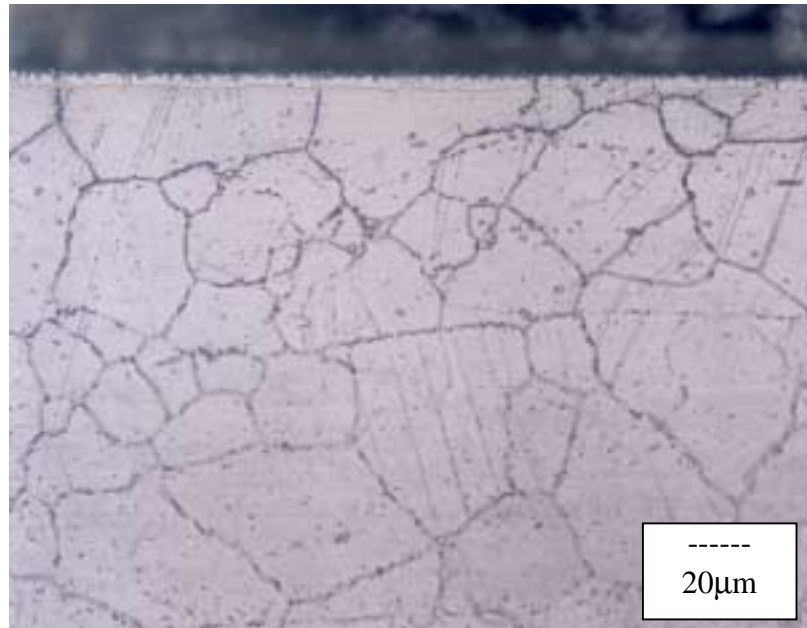


Figure 10. Photomicrographs showing alloy 617 after 14,160 hours of exposure in CO-20% H₂ at 621°C. The sample was electrolytically etched in methanol - 5% HNO₃. The top photo shows the microstructure of the general surface, which exhibited a thin layer presumed to be carbide. While only shallow pitting (less than 50 microns) was observed on the general surface, the corners of the sample were attacked (bottom photo).

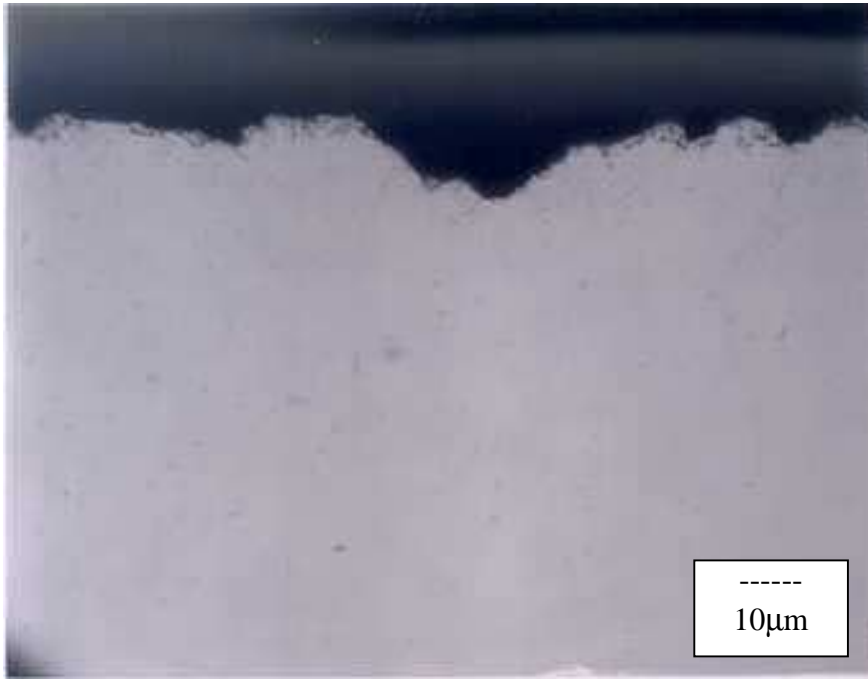


Figure 11. Photomicrograph showing the surface of alloy 693 after 15, 816 hours of exposure in CO-20% H₂ at 621°C.